Directional visible light communication signal enhancement using a varifocal micromirror with four degrees of freedom

Jessica Morrison[1], Michael Rahaim[2], Yun Miao[3], Matthias Imboden[4], Thomas D.C. Little[2], Valencia Koomson[3], and David J. Bishop[1,2,5]

[1]Department of Physics, Boston University, Boston, MA 02215, USA
[2]Department of Electrical and Computer Engineering, Boston University, Boston, MA 02215, USA
[3]Department of Electrical Engineering, Tufts University, Medford, MA 02155, USA
[4]Microsystems for Space Technologies Laboratory, École Polytechnique Fédérale de Lausanne (EPFL), Neuchâtel, Switzerland
[5]Division of Materials Science and Engineering, Boston University, Brookline, MA 02446, USA

ABSTRACT

We present the use of a micromirror to dynamically improve an optical wireless communiciations link. The signal-to-noise ratio (SNR) is improved by directing the output of a 675 nm laser diode modulated at 10 MHz toward a receiver and by varying the divergence of the output beam using a varifocal, tip-tilt-piston micromirror. The SNR has a dynamic range of 30 dB for a diffuse source, all by optimizing the overall shape and direction of the mirror.

Keywords: Solid state lighting, microelectromechanical systems, MEMS, visible light communications, optical wireless communications, lasers, LEDs

1. INTRODUCTION

Next generation communications systems are moving toward synergistic dual use regimes in which personal access points are sourced from existing architectures. Optical Wireless Communications (OWC) has the capacity to introduce small cell, user specific data links. The introduction of steerable OWC pushes the envelope in transforming communications toward high data rates and low signal interference while accommodating user mobility.

We discuss the use of a single microelectromechanical system (MEMS) micromirror[1] with both adaptive focus and large range angular deflection in OWC. A laser diode, focused and directed toward the micromirror, is modulated using On-Off-Keying (OOK) at 20 Mb/s using a 10 MHz square wave. However, data rates on the order of Gb/s have been obtained by direct modulation of laser diodes.[2–4] In this paper we compare the signal quality based on beam shape and direction. Therefore, lower data rates are acceptable and can be improved upon with a high speed source.

The modulated signal reflected from the micromirror is detected using an avalanche photodiode (APD) at a distance of 3 m from the micromirror. Upon reflection from the micromirror, the divergence of the light can be tuned anywhere from 20° to a collimated source and steered along two axes up to ±30°. Thus, the range in signal strength is highly dependent on the focal length and direction of the mirror. At a minimum, the signal is below the noise level but by directing the signal toward the detector and optimizing the focal length of the mirror, the signal-to-noise ratio (SNR) can be improved in a diffuse lighting environment by more than 30 dB.

Fifteenth International Conference on Solid State Lighting and LED-based Illumination Systems, edited by Matthew H. Kane, Nikolaus Dietz, Ian T. Ferguson, Proc. of SPIE Vol. 9954, 99540C · © 2016 SPIE · CCC code: 0277-786X/16/$18 · doi: 10.1117/12.2237736

2. OPTICAL WIRELESS COMMUNICATIONS

OWC is a form of optical communication that uses the visible, infrared (IR) or ultraviolet (UV) spectrum for wireless data transfer in free space. In most cases, intensity modulation with direct detection (IM/DD) is utilized such that information is embedded within the modulated optical intensity and received via direct conversion of the received optical power to an electrical current. Highly directional point to point OWC links have been implemented over large distances via free-space optical communication (FSO) for many years - including building to building and satellite communications. More recently, interest in indoor OWC has grown due to the demand for ultra dense wireless communications stemming from an increasing number of wireless devices and increasing requirements from applications that utilize wireless connectivity.

The idea of indoor OWC was presented in regards to IR as early as 1979[5] and witnessed a resurgence in the late 1990's[6,7] as a potential wireless local area network (WLAN) technology. Improvements in light emitting diode (LED) technology and adoption of LED-based lighting drew attention to dual-use lighting and communication systems implementing visible light communication (VLC) in the 2000's.[8–10] This led to research in high speed VLC systems achieving data rates well beyond 1 Gbps,[2–4] standardization efforts for VLC modulation and coding schemes,[11] and interest in VLC as a component of the 5G ecosystem.[12,13]

While much of the work in the field of VLC has focused on transmission via broad emission luminaires, indoor VLC-based FSO systems offer flexibility in the optical emission pattern while maintaining the possible integration of FSO in existing fixtures. Previous work on adaptable indoor OWC includes transmitters with adaptive lenses[14] and a combination of adaptive transmitters and receivers.[15] An FSO system has been built and tested using a commercial MEMS mirror together with an adjustable lens unit.[16] However, all of the adaptive components require a mechanical adaptive focus separate from the steering component. The integration of variable focus and steering can drastically improve alignment costs and viability for indoor FSO systems on a large scale.

Given the ability to adapt the emission pattern and direction of an optical source, link performance can be improved by increasing the optical signal power directed towards a receiver and maximizing the optical SNR. Accordingly, the analysis presented in this work evaluates SNR for various divergence and steering angles. In indoor FSO networks with many access points and user devices, aggregate performance is also improved by minimizing interference between OWC links. The lighting mission in dual-use VLC systems requires near-uniform illumination; therefore, broad emission VLC luminaires are often provisioned with overlapping cells. In such systems, resources are divided to mitigate interference. Narrow emission optical sources in an indoor FSO system allow for full reuse of resources in scenarios where user devices are densely located; however, signal acquisition becomes more challenging. The evaluation of multi-cell / multi-user OWC systems is beyond the scope of this paper; however the presented results indicate how variable divergence angle can provide narrow emission for increased SNR and interference mitigation while also providing broader emission capabilities for simplified acquisition.

2.1 Signal Constraints

When evaluating performance of a digital communications link, SNR is often used as a metric for channel quality. Accordingly, SNR is defined in relation to the signal constraints such that a fair comparison can be made between various implementations.

Conventionally, average electrical signal power is observed since the signal in wireline or RF communications is subject to a power constraint in the form $E\left[X_e^2(t)\right] \leq C_1$ where X_e is the electrical signal (i.e., voltage or current), C_1 is proportional to the maximum electrical power, and $E[\cdot]$ is the expected value operator.

In OWC, average optical power is often constrained due to eye safety regulations or lighting requirements. This constraint is in the form $E[X_o(t)] \leq C_2$ where X_o is the optical signal and C_2 relates to the average transmitted optical power. Therefore, the average signal is commonly observed for fair comparison in OWC.

Optical power is constrained to positive values and transmitters have a maximum instantaneous optical power; therefore the transmitted optical signal is also subject to the constraint $0 \leq X_o(t) \leq C_3$ where C_3 is

the maximum instantaneous transmitted optical power. Since optical power is directly related to electrical current in IM/DD systems, the peak to peak signal range is observed. In this work, we observe the peak to peak constraint in order to highlight relative performance of the device configurations irrespective of the lighting mission.

2.2 Noise

There are various noise components in an OWC link, each conventionally assumed as zero-mean additive white Gaussian noise (AWGN) for simplicity of analysis. Given this assumption, the aggregate noise can be modeled as a zero-mean AWGN source with variance, σ_n^2, equal to the sum of the variances from each of the components. The dominant noise components in OWC are typically shot noise and thermal noise, therefore:

$$\sigma_n^2 = \sigma_{n,shot}^2 + \sigma_{n,therm}^2 \tag{1}$$

Depending on the characteristics of the receiver, the noise may be shot-noise or thermal-noise dominant. Noise power is independent of the signal in the later case; however, shot noise is dependent on the amount of light that lands on the receiver - including ambient light and light from the signal source. Accordingly, evaluation of systems that are affected by shot noise should account for differences in the noise power between symbols. Since the optical power from ambient light is much larger than the received optical power from the source in many VLC systems, shot noise power is often assumed to be constant. However, signal-dependent noise characterization is important for scenarios such as indoor FSO where the received optical signal power is on the same order of magnitude or larger than the ambient light power.

In the analysis within this paper, we evaluate noise power at each mirror configuration. The measurements are taken by pulling a 25 ns window at the center of the expected high and low time windows. Then the variance in high and low measurements, written as σ_0^2 and σ_1^2 respectively, and corresponding means are calculated over 200 periods. Assuming the noise power does not depend on the symbol, the variance of the high and low measurements are approximately equal and are calculated as such. In certain extreme cases, we encounter unexpectedly high noise power fluctuations. This is discussed in more detail in Section 4.

2.3 Signal to Noise Ratio

When evaluating performance, the observed SNR definition depends on the signal constraints. Since performance is evaluated at the receiver, transmit constraints are observed in relation to the received electrical signal current, $I_s(t)$.

In the case of an average electrical power constraint, SNR is defined such that the ratio of electrical signal power, $P_{e,sig}$ to electrical noise power, $P_{e,n}$ is the trait used to compare performance. The variance of the assumed zero mean signal is equivalent to the mean of the squares and load resistance is assumed to be the same for signal and noise; therefore

$$SNR_{P_e} = \frac{P_{e,sig}}{P_{e,n}} = \frac{E\left[I_s(t)^2\right]}{E\left[I_n(t)^2\right]} = \frac{\sigma_{I_s}^2}{\sigma_n^2} \tag{2}$$

where $I_n(t)$ is the received noise current with variance σ_n^2.

When observing a peak to peak constraint, the trait to be held constant is the range of the received optical signal power, $P_{o,p-p}$, which is directly related to the range of the received electrical signal current, $I_{s,p-p}$. Accordingly, peak-to-peak SNR is defined as

$$SNR_{p-p} = \frac{RP_{o,p-p}}{I_{n,rms}} = \frac{I_{s,p-p}}{\sigma_n} \tag{3}$$

where R is the photosensor responsivity [A/W]. Note that the noise standard deviation is observed in the denominator such that SNR_{p-p} is unitless.

In this paper, SNR_{p-p} is presented for comparison of the mirror configurations. Since the received optical power is dependent on the power density of the optical signal incident on the surface of the photosensor, directing the emitted signal towards the receiver and focusing the emitted optical power maximizes $P_{o,p-p}$ for a given transmitted optical power. The presentation of the SNR is given in dB calculated using the electrical power convention where

$$SNR_{p-p}\,[\text{dB}] = 20\log_{10}\left(\frac{I_{s,p-p}}{\sigma_n}\right) \tag{4}$$

In the analysis of symbol error rate (SER) in optical communications, it is assumed that the symbol constellation is translated to incorporate a bias such that the positive value constraint is met. When SER is calculated as a function of SNR_{p-p}, the distance between symbols is related to the peak to peak received signal current, $I_{s,p-p}$, which is independent of DC bias. For OOK, there are 2 equidistant symbols over the range $I_{s,p-p}$; therefore $d = I_{s,p-p}$. An error occurs if the noise current, I_n, shifts the observed signal current by at least $d/2$ towards another symbol. Positive or negative noise current with magnitude greater than $d/2$ occurs with equal probability given that I_n is normally distributed, $\bar{I}_n = 0$; therefore assuming I_n is not symbol dependent,

$$\begin{aligned} P\left(I_n \geq \frac{d}{2}\right) &= P\left(I_n \leq \frac{d}{2}\right) = Q\left(\frac{d}{2\sigma_n}\right) \\ &= Q\left(\frac{I_{s,p-p}}{2\sigma_n}\right) = Q\left(SNR_{p-p}\right) \end{aligned} \tag{5}$$

where Q is the complimentary error function. Based on the noise assumptions outlined in Section 2.2, an error occurs when $I_s = 0$ and $I_n \geq d/2$ or when $I_s = 1$ and $I_n \leq -d/2$. Given equiprobable symbols and assuming noise is independent of the symbol,

$$BER_{OOK} = P\left(I_n \geq \frac{d}{2}\right) = Q\left(SNR_{p-p}\right) \tag{6}$$

3. PROTOTYPE TRANSMITTER

The transmitter is composed of two main systems. The first is a MEMS micromirror described in detail in Section 3.1. The second is a bare laser diode connected to a printed circuit board (PCB) containing a reference input and constant current controller. The laser system is outlined in Section 3.2 and can be expanded to achieve Gb/s modulation rates.

3.1 Micromirror System

This section describes the mirror design and fabrication process as well as the electrothermal actuation method used to control the mechanical deformation with four degrees of freedom.

The mirror is built using a multi-user MEMS process known as PolyMUMPS by MEMSCAP. The architecture is based on three poly-silicon layers and one gold layer. Two sacrificial oxide layers allow suspended structures to be fabricated out of the top two poly-silicon layers. The gold is deposited on the top silicon layer and can be used for electric access and to fabricate vertical actuators. A comprehensive description of the layers, fabrication process and design tolerances is given in the PolyMUMPs handbook.[17]

The deformable MEMS mirror used in this work is illustrated in Figure 1. The device consists of four thermal bimorph legs and a central mirror. The bimorph legs are composed of 0.5 μm gold on 1.5 μm of poly-silicon. Compressive stress in the silicon and tensile stress in the gold from the fabrication process results in a curved structure which is used to raise the mirror above the plane. Thermal annealing protocols are used to maximize the curvature at ambient temperature. To actuate the device, a constant current can be injected within each leg independently. The resulting Joule heating ($P = I_{mir}^2 R$) will raise the temperature along

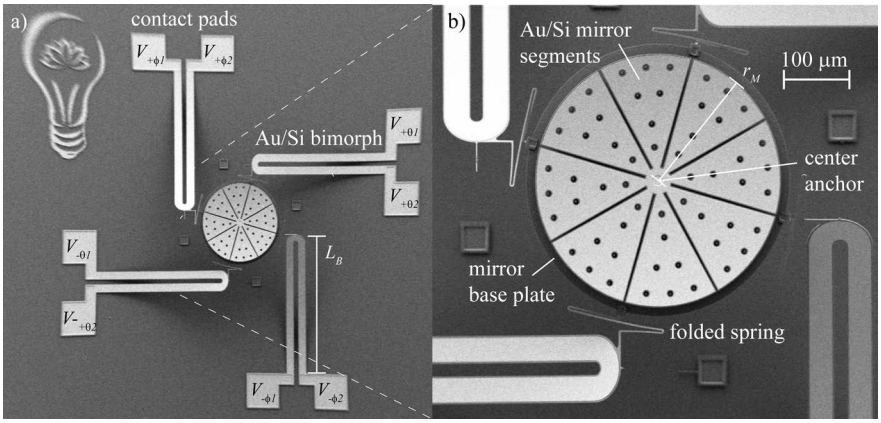

Figure 1. SEM image of the MEMS Mirror. a) Mirror device consists of a segmented mirror with a tunable focal length and four thermal bimorphs that can perform tilt, tip, and piston deformations. b) Closeup of segmented mirror with eight petals. Dark circles are release holes.

the structure and straighten the bimorph leg. Following Chu *et al.*,[18] a uniform temperature increase will provide a bending moment due to the mismatch in coefficients of thermal expansion (CTE). The curvature, κ, is the inverse of the radius of curvature and twice the focal length, $r = 2 \cdot f$, and can be expressed as the sum of the initial curvature and a temperature dependent term proportional to both the change in temperature, ΔT:

$$\kappa = \frac{1}{r} = \frac{1}{r_0} + \frac{6t\left(\alpha_{Au} - \alpha_{Si}\right)\Delta T}{4(t_{Au}^2 + t_{Si}^2) + 6t_{Au}t_{Si} + \frac{E_{Au}t_{Au}^3}{E_{Si}t_{Si}} + \frac{E_{Si}t_{Si}^3}{E_{Au}t_{Au}}}. \tag{7}$$

Here, α_i, t_i and E_i is the CTE, thickness, and Young's modulus of the gold and poly-silicon respectively.

The mirror assembly is tethered to the four bimorphs by folded springs. These poly-silicon springs have a sufficiently low spring constant to allow the bimorph beams to deflect and thereby tip or tilt the mirror. The mirror itself is segmented into eight sections, anchored at the center to a poly-silicon platform. The segments are composed of the same thin films as the bimorph legs and will likewise have an initial curvature, resulting in a spherical mirror that can focus (or defocus) light. The mirror temperature can be raised by applying a voltage across the folded springs. These act as four heat sources, causing the platform to uniformly heat the mirror segments. The temperature of the plate can be raised sufficiently to completely flatten the mirror, corresponding to an infinite focal length.

The gold in the bimorph legs makes their electrical and thermal resistances low, where the long narrow silicon springs have greater electrical and thermal resistances. This allows the central platform and legs to be heated independently. Injecting a current into a single bimorph will deflect the structure in the direction of actuated bimorph. Heat can be generated in the springs by providing a voltage between the bimorph legs from 0 V to 15 V. At 0 V, the mirror is curved such that the focal length is near $f = -0.5$ mm. At 15 V, the focal length is nearing infinity and can be approximated as a flat mirror. The bimorph legs and mirror segments can be actuated independently with little impact on one another. The interested reader is referred to a detailed description of a similar device, including range, power consumption, mirror shape, and dynamic response, by Morrison *et al.*[1]

3.2 Laser Source and Driver

Figure 2(left) shows the schematic of the laser driver. The laser driver is composed of a high power gallium arsenide (GaAs) field effect transistor (FET), a current control loop, a laser diode, and a high speed modulator. The current sensing resistor R1 and the amplifier A1 form a negative feedback loop to stabilize the DC current flowing through the laser diode. A GaAs pseudomorphic high-electron-mobility transistor (Avago

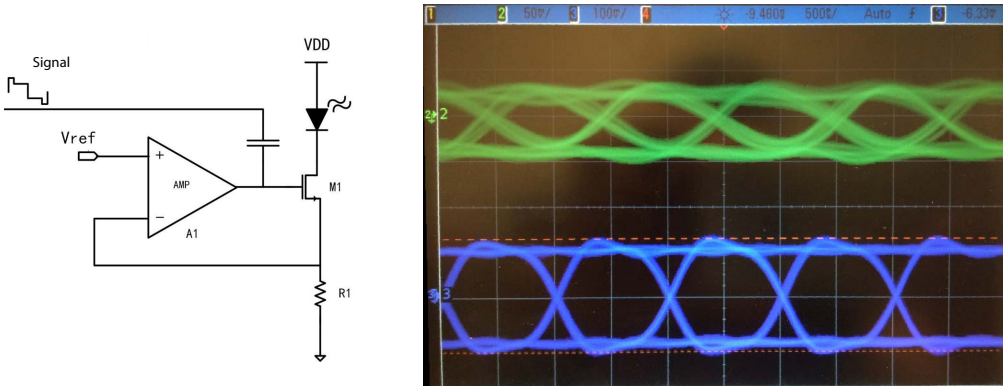

Figure 2. Schematic of the laser driver (left) and eye diagrams (right) of PRBS generator output (blue) and received data (green) from a commercial detector at 1 Gb/s. The laser diode and detector for this high speed test are separated by 15 cm without optics.

ATF541M4) with 6 GHz bandwidth and 100 mA current capability is used as the main driver to support high speed modulation and high level optical power. The laser diode (Thorlabs HL6750MG) emits at 675 nm with a 50 mW maximum output power is connected to an adapter for lens installation. The adapter can also serve as a heat sink, when thermal equilibrium is reached the adapter and the feedback loop can guarantee a constant average optical power output.

As shown in Figure 2(right) the laser driver can maintain a clear eye pattern up to 1 Gb/s. It should be mentioned that the current setup is modulated at a much lower frequency than the maximum allowable by the electronics. This is to allow the use of a standard arbitrary function generator which has a maximum output frequency of 15 MHz.

4. RESULTS

4.1 Measurement Setup

A square wave input function modulated at 10 MHz is used to drive the laser described in Section 3.2. A DC bias is added in order to provide symmetric bias current nearing the threshold current. Directly in line with the laser diode is a collimating lens followed by an adjustable iris. The function of the iris is primarily to reduce internal reflections from the diode cavity from being directed toward the MEMS system. A focusing lens immediately follows the iris and focuses the light passing through the iris onto the mirror.

The MEMS device is mounted on a standard 16 pin dual-inline package which is oriented at a 45° angle with respect to the incoming beam. The reference bias is held at 1.5 V corresponding to a 31 mA forward current, just above the lasing threshold. The laser used is capable of providing up to 50 mW but the maximum intensity is not desired for this use. The average total optical intensity is kept near the threshold in order to remain eye safe. The modulation depth is also relatively low because large modulation depths will saturate the photodetector used in this experiment. The preliminary measurements in the next section 4.2 describe the results when using a larger maximum optical power.

Signal power is shown to improve by a factor of four for a low intensity diffuse signal. When the signal is not first passed through a diffuser, the power can be improved by a factor of 15. However, a factor of 15 improvement in signal comes with penalties in SNR.

The state of the micromirror is given in terms of the mirror voltage (in the legend and varies from 0 V to 15 V) which increases with increasing focal length.[1] When the mirror is at 0 V, the focal length is approximately $f \approx -1$ mm leading to a divergent beam. When the voltage is at 15 V, the focal length is set such that the outgoing beam is effectively collimated. Similarly, the beam direction is proportional to the square of the current $\left(\theta \propto P_{mir} \propto I_{mir}^2 R_{mir}\right)$ and is written as such in all plots.

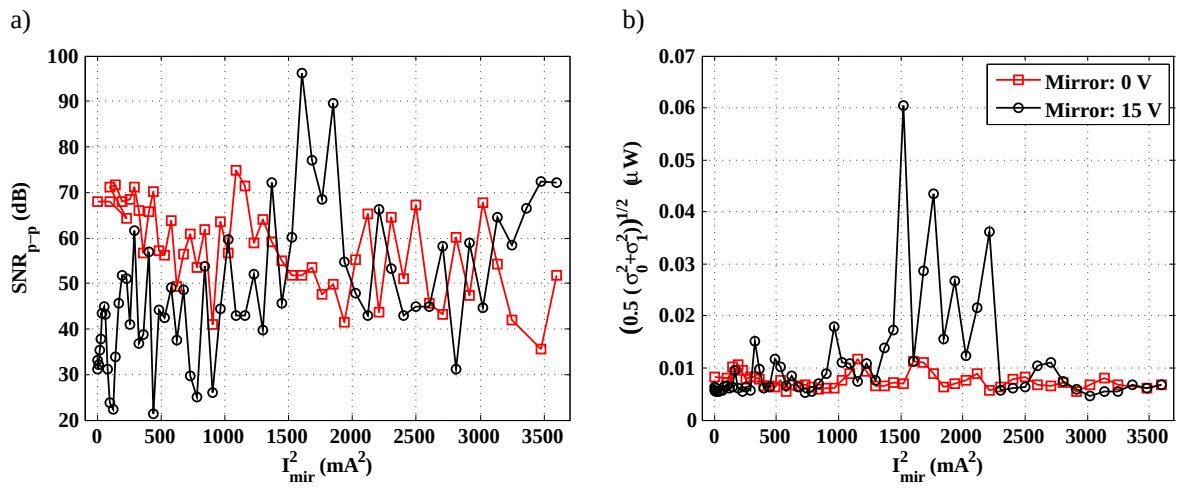

Figure 3. Signal-to-noise ratio (a) for a mirror with a divergent reflected beam (Mirror: 0 V) and for the mirror when the beam is approximately collimated (Mirror: 15 V) as a function of effective beam direction. The significant drop in SNR for a collimated beam is due to a substantial increase in the noise (b).

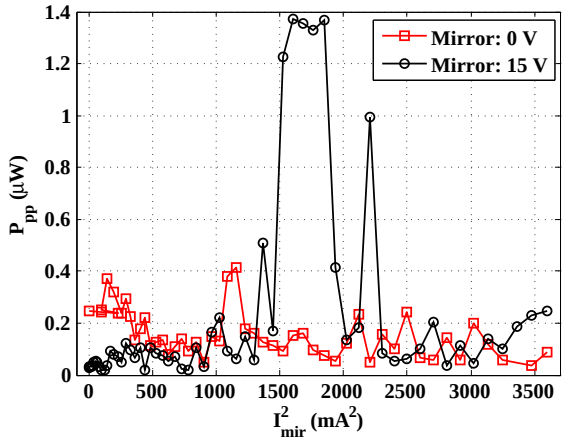

Figure 4. Total optical power received by the photodetector as the mirror is deflected measured for both a divergent and a collimated beam.

4.2 Preliminary Measurements

Preliminary measurements demonstrate an improvement in SNR from 20 dB to 97 dB when the mirror is effectively flattened so the reflected light is close to collimated. However, this improvement is at the maximum optical power threshold for the photodetector. The penalty for operating at the power density required to obtain 97 dB SNR is an increase in noise levels. Figure 3 shows the enhanced SNR as a function of the beam direction.

Between $I^2_{mir} = 1500$ mA^2 and $I^2_{mir} = 1800$ mA^2 the detector saturated (Figure 4). As a result, the SNR at these points are not a good measure of signal quality but the overall maximum amplitude improvement from beamshaping (i.e. changing the focal length of the mirror) is clear.

Another issue with the direct line measurements are blackout spots. The release holes in the mirror segments can be seen as dark circles in Figure 1. These are physical holes in the mirror in order to aid

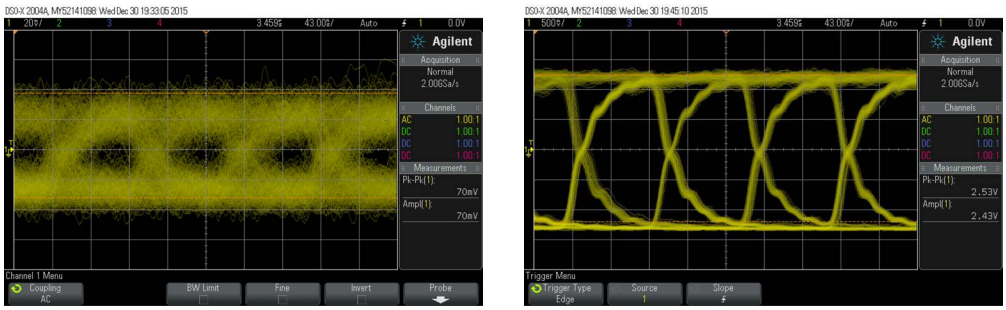

Figure 5. Eye diagrams for a poorly aligned system (left) and optimally aligned system (right) just before saturation of the photodiode.

in processing times and reduce optical aberrations due the stress gradients from the overall shape of the segments. Each of the holes and corresponding interference patterns can be seen in the reflected light. As the reflection is swept across the detector, blackout spots can be seen where the signal power suddenly drops (Figure 4).

Using a 10 Mb/s PRBS signal, eye diagrams for the same type of setup are shown in Figure 5. The leftmost diagram is the signal for a divergent beam prior to redirecting the signal toward the detector. The second is the best signal obtained by collimating the beam and redirecting just before saturating the signal. The opening is drastically shifted upon optimizing the beam shape and direction. The exact culprit responsible for the noise amplification is likely an artifact of the saturation limit in the photodetector and an investigation into this is left for future work. Instead, a lower optical power is used in conjunction with a diffusive element to reduce the total optical power detected by the sensor.

4.3 Diffuse Signals

The diffuser inserted to measure low optical power signals has two functions. The first is to reduce the level of contrast in the mirror image to smooth the transitions across the release holes and interference patterns. The second is to decrease the optical power density on average. In effect, the diffuser shifts the range in divergence of the beam so the variable focus will still control the power density but with an initial offset to prevent collimated light from reaching the detector.

Figure 6(a) depicts the optical power measured by the photodiode as a function of the effective direction. The blackout areas are now smoothed over as is expected when using the diffuser to reduce the projected image of the mirror. In addition, the photodetector is far from saturation and the noise 6(b) as a function of direction is much less erratic. While the signal enhancement is not as notable as in the preliminary work, the results seem to be more reliable and less dependent on the signal itself.

Eye diagrams in Figure 7 show the eye opening from a diffuse signal without direction (a) to a narrow beam incident on the diffuser directed at the detector (b). These are data from a square wave that are pulled from the oscilloscope rather than an image of the oscilloscope panel itself.

Since the noise level does not vary as significantly as shown in Figure 3(b), the SNR shown in Figure 8(a) steadily rises as the signal is directed toward to the detector. The gradient in SNR is largest when the mirror is flattened and peaks at approximately 65 dB. When the mirror is left divergent but still directed toward the detector, the SNR drops to 40 dB. When the signal is pointed away from the detector, $\left(I_{mir}^2 = 3600\,\mathrm{mA}^2\right)$, the SNR drops to 35 dB regardless of the curvature of the mirror. The baseline is an artifact of the final direction of the mirror relative to the detector position and will continue to decrease if the mirror current is increased further.

In order to obtain a worst case SNR, a second ratio is derived based on the noise at the peak amplitude. As described in Section 2, for large optical powers the shot noise component may increase such that the

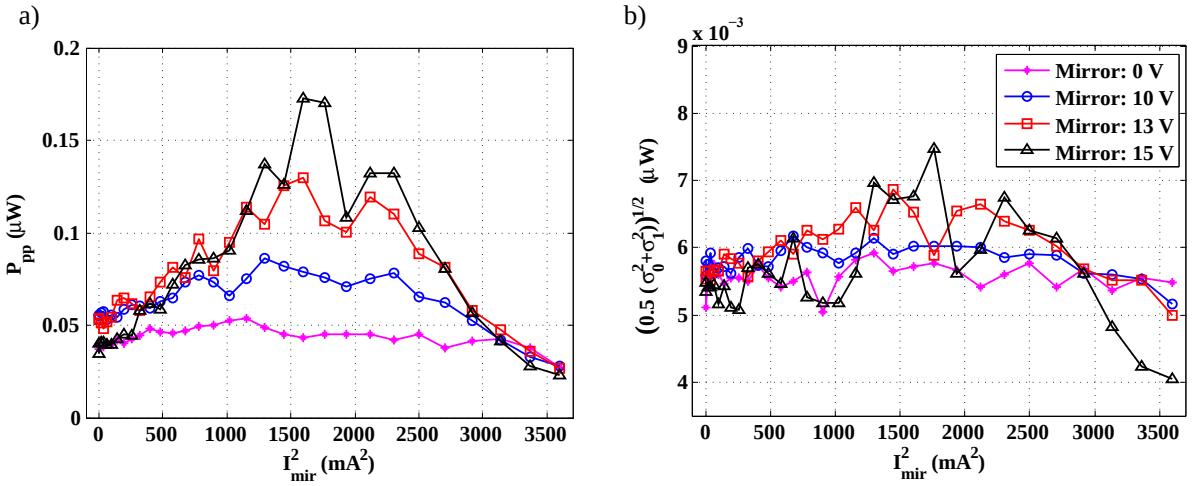

Figure 6. Optical power incident on the photodiode (a) is shown as a function of the effective direction of the signal for a series of mirror focal lengths. In (b) the total noise is reduced in comparison to the values in the preliminary data.

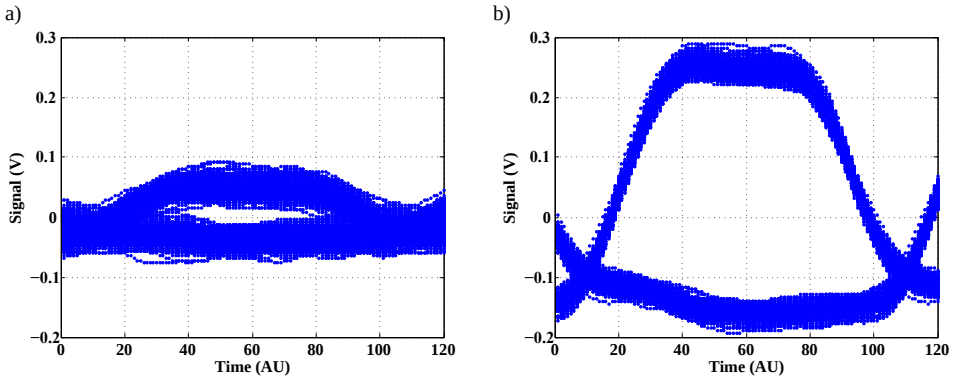

Figure 7. Eye diagrams for an indirect signal with a divergent beam incident on the diffuser (a) and for a direct line signal with a collimated beam incident on the diffuser (b).

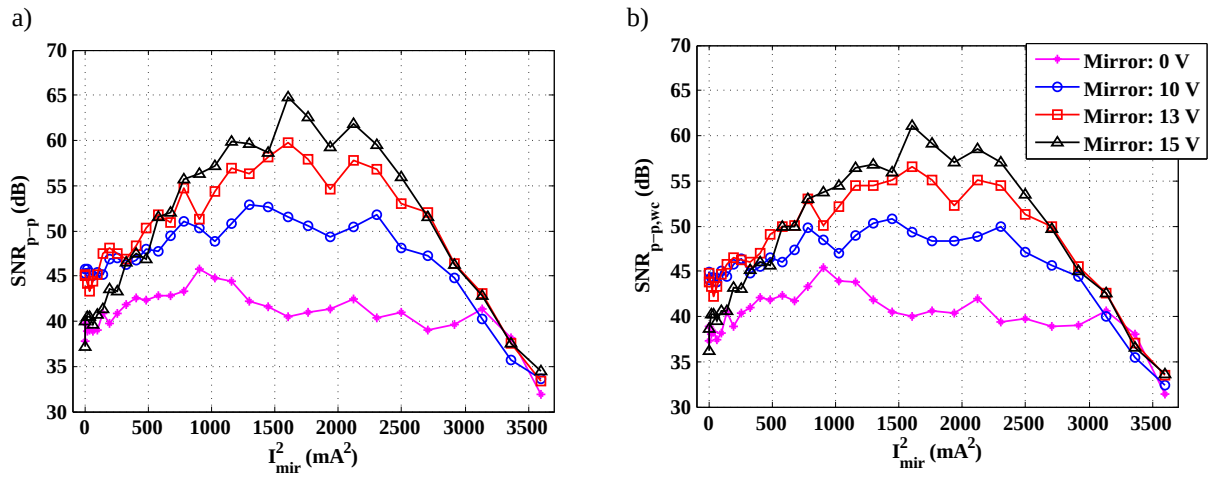

Figure 8. The SNR improves as the beam direction is shifted toward the detector. The improvement is accentuated by increasing the focal length of the mirror. This is shown in the case of symbol independent noise (a) and assuming the noise is always given by σ_1 (b).

noise is symbol dependent. Thus, for a square wave the noise will always be greater during the half of the period corresponding to a high measurement. By assuming the noise is always given by the shot noise dominant component, the SNR is defined by $SNR_{pp,wc} = \frac{P_{pp}}{\sigma_1}$ rather than by the average noise variance $SNR_{pp} = \frac{P_{pp}}{\sqrt{\frac{1}{2}\left(\sigma_1^2+\sigma_0^2\right)}}$. As a result, the SNR is unchanged for a wide beam angle (Mirror: 0 V) but drops by 4 dB for a collimated beam incident on a diffuser (Mirror: 15 V). The overall shift is plotted in Figure 8(b).

Based on the SNR calculations in Figure 8, the BER can be extrapolated using Equation (6). From this the calculated BER is far below a measurable value, $BER < 10^{-9}$. This demonstrates that the bit errors would be systemic rather than an artifact of the noise level. Far greater is the impact of a pre-shaped beam than one which is directed but highly divergent on the SNR.

5. CONCLUSIONS

Signal enhancement using a 675 nm laser diode incident on a multi-degree of freedom micromirror can be as great as $\Delta SNR = 77$ dB. However, useful ranges can be obtained by inserting a diffusive element which will drop the enhancement dynamic range to within limits suitable for an indoor FSO system. The SNR for such a system can be shifted from less than 35 dB to $60 - 65$ dB by redirecting the beam and reshaping it before the diffuser. Both of these variations are performed with a single micromirror at voltages well below standard wall plug limits.

While one can certainly begin with a collimated beam on a diffuser without losing dynamic range in the signal, the added flexibility will allow reconfigurable OWC networks. Enhancing signal and providing a basis for reshaping the optical system with a single mirror may also have implications on the reduction of interference between nearby transmitters and on user mobility in indoor FSO.

ACKNOWLEDGMENTS

This work was supported primarily by the Engineering Research Centers Program of the National Science Foundation under NSF Cooperative Agreement No. EEC-0812056. Any opinions, findings and conclusions or recommendations expressed in this material are those of the author(s) and do not necessarily reflect those of the National Science Foundation.

REFERENCES

[1] Morrison, J., Imboden, M., Little, T. D. C., and Bishop, D. J., "Electrothermally actuated tip-tilt-piston micromirror with integrated varifocal capability," *Opt. Express* **23**(7), 9555 (2015).

[2] Chi, Y.-C., Hsieh, D.-H., Tsai, C.-T., Chen, H.-Y., Kuo, H.-C., and Lin, G.-R., "450-nm GaN laser diode enables high-speed visible light communication with 9-Gbps QAM-OFDM," *Opt. Express* **23**(10), 13051 (2015).

[3] Chi, Y.-C., Hsieh, D.-H., Lin, C.-Y., Chen, H.-Y., Huang, C.-Y., He, J.-H., Ooi, B., DenBaars, S. P., Nakamura, S., Kuo, H.-C., and Lin, G.-R., "Phosphorous Diffuser Diverged Blue Laser Diode for Indoor Lighting and Communication," *Sci. Rep.* **5**, 18690 (2015).

[4] Janjua, B., Oubei, H. M., Retamal, J. R. D., Ng, T. K., Tsai, C.-T., Wang, H.-Y., Chi, Y.-C., Kuo, H.-C., Lin, G.-R., He, J.-H., and Ooi, B. S., "Going beyond 4 Gbps data rate by employing RGB laser diodes for visible light communication," *Opt. Express* **23**(14), 18746 (2015).

[5] Gfeller, F. R. and Bapst, U., "Wireless in-house data communication via diffuse infrared radiation," *Proceedings of the IEEE* **67**, 1474–1486 (1979).

[6] Park, H. and Barry, J., "Modulation analysis for wireless infrared communications," in [*Communications, 1995. ICC '95 Seattle, 'Gateway to Globalization', 1995 IEEE International Conference on*], **2**, 1182–1186 vol.2 (1995).

[7] Kahn, J. and Barry, J., "Wireless infrared communications," *Proceedings of the IEEE* **85**, 265 –298 (1997).

[8] Komine, T. and Nakagawa, M., "Fundamental Analysis for Visible-Light Communication System Using LED Lights," *Consumer Electronics, IEEE Transactions on* **50**, 100 – 107 (2004).

[9] Elgala, H., Mesleh, R., Haas, H., and Pricope, B., "OFDM Visible Light Wireless Communication Based on White LEDs," in [*Vehicular Technology Conference, 2007. VTC2007-Spring. IEEE 65th*], 2185 –2189 (2007).

[10] Little, T. D. C., Dib, P., Shah, K., Barraford, N., and Gallagher, B., "Using LED lighting for ubiquitous indoor wireless networking," in [*IEEE WiMob 2008.*], 373–378 (2008).

[11] IEEE, "802.15.7-2011 - ieee standard for local and metropolitan area networks: Short-range wireless optical communication using visible light," (2011).

[12] Hanzo et al., "Wireless myths, realities, and futures: From 3G/4G to optical and quantum wireless," *Proc. of the IEEE* **100**, 1853–1888 (2012).

[13] Rahaim, M. B. and Little, T. D. C., "Toward practical integration of dual-use vlc within 5g networks," *IEEE Wireless Communications* **22**, 97–103 (2015).

[14] Wang, K., Nirmalathas, A., Lim, C., and Skafidas, E., "High-speed duplex optical wireless communication system for indoor personal area networks.," *Opt. Express* **18**(24), 25199–25216 (2010).

[15] Zhang, X., Tang, Y., Cui, L., and Bai, T., "Continuous zoom antenna for mobile visible light communication," *Appl. Opt.* **54**(32), 9606 (2015).

[16] Brandl, P., Schidl, S., Polzer, A., Gaberl, W., and Zimmermann, H., "Optical Wireless Communication With Adaptive Focus and MEMS-Based Beam Steering," *IEEE Photonics Technol. Lett.* **25**(15), 1428–1431 (2013).

[17] Cowen, A., Hardy, B., Mahadevan, R., and Wilcenski, S., [*PolyMUMPs Design Handbook*], MEMSCAP Inc., 13.0 ed. (2011).

[18] Chu, W.-H., Mehregany, M., and Mullen, R. L., "Analysis of tip deflection and force of a bimetallic cantilever microactuator," *Journal of Micromechanics and Microengineering* **3**(1), 4 (1993).